configuration where the particle normal stays perpendicular to the magnetic field. Additionally, several factors of the clay water system, such as gelation and long range colloidal interactions, makes the nematic phase in a clay suspension different from ordinary liquid crystals. From the images of the evolution of the periodic patterns (Figure 1) it can be seen that the stripe formation commences at the top of the nematic sol, close to the isotropic-nematic interface. This could be due to a viscosity gradient in the nematic sol along the capillary axis, i.e. lower viscosity near the isotropic-nematic interface and highest near the transition to the nematic gel.

Figure 2 shows repeated measurements with identical samples, using magnetic fields from 0.5 to 1 Tesla. The threshold value for the inhomogeneous Frederiks transition with this setup is found to be just below 0.5 Tesla. Because of irregularities in the nematic domains, and the limited extent of the nematic sol region, it is with the present samples not possible to obtain precise values for the wavelength for a specific magnetic field strength. However, it seems clear that there is a decrease in wavelength when the magnetic field is increased, and close to 0.5 Tesla, the wavelength looks to diverge, as expected.

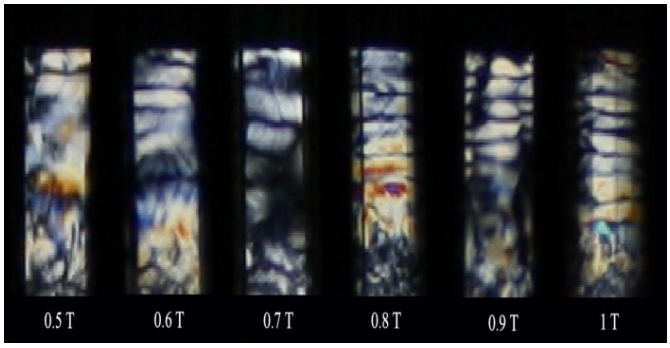

Figure 2: Stripe patterns for magnetic fields from 0.5 to 1 Tesla in the same sample. The pictures were taken at the point in time when the stripes were most clearly defined.

For all the measurements the wavelength shows a tendency to increase as we move down in the sample, which could be due to a viscosity gradient in the nematic gel as the concentration of particles in the nematic sol increases downwards. Furthermore, the duration of the instability decreases with increasing field strengths: the whole process lasts for over 3 hours with magnetic fields close to the threshold, and under 2 hours for fields of 1 Tesla. For low field strengths, the first sign of stripe formation appears after 10 minutes, while for the highest strengths it can take less than five minutes. The periodic structures are clearly transient phenomena, and are seen to decay soon after the magnet is removed. The lifetime is around 2 hours after which there is no longer any pattern with systematic structure.

[1] A. Repiova and V. Frederiks, J. Russ. Phys.-Chem. Soc. **59**, 183 (1929).
[2] P. G. d. Gennes and J. Prost, *The physics of liquid crystals* (Oxford University Press, Oxford, 1993), pp. xvi.
[3] A. J. Hurd, S. Fraden, F. Lonberg, and R. B. Meyer, J. Phys-Paris **46**, 905 (1985).
[4] Z. Dogic and S. Fraden, Langmuir **16**, 7820 (2000).
[5] D. van der Beek, P. Davidson, H. H. Wensink, G. J. Vroege, and H. N. W. Lekkerkerker, Phys. Rev. E **77**, 031708 (2008).
[6] M. R. Kuzma, Phys. Rev. Lett. **57**, 349 (1986).
[7] H. Hemmen, N. I. Ringdal, E. N. De Azevedo, M. Engelsberg, E. L. Hansen, Y. Meheust, J. O. Fossum and K. D. Knudsen, Langmuir **25**, 12507 (2009).
[8] N. I. Ringdal, D. M. Fonseca, E. L. Hansen, H. Hemmen, and J. O. Fossum, Phys. Rev. E **81**, 2010).
[9] J. C. P. Gabriel, C. Sanchez, and P. Davidson, J. Phys. Chem. **100**, 11139 (1996).
[10] L. J. Michot, I. Bihannic, S. Maddi, S. S. Funari, C. Baravian, P. Levitz, and P. Davidson, Proc. Natl. Acad. Sci. U.S.A. **103**, 16101 (2006).
[11] E. N. de Azevedo and M. Engelsberg, Langmuir **25**, 1175 (2009).
[12] M. Kildemo, L. M. S. Aas, P. G. Ellingsen, H. Hemmen, E. L. Hansen and J. O. Fossum, Proc Spie, **8082**, 808221 (2011).

INTERMITTENCY OF FLUID IMBIBITION IN DISORDERED MEDIA

INTERMITENCIA EN "EMBEBIMIENTO" FLUIDO EN MEDIOS DESORDENADOS

X. Clotet[a,b], S. Santucci[a,c †] and J. Ortín[b]

a) Laboratoire de Physique, CNRS UMR 5672, Ecole Normale Supérieure de Lyon, 46 Allée d'Italie, 69364 Lyon Cedex 07, France, stephane.santucci@ens-lyon.fr†
b) Departament d'Estructura i Constituents de la Matèria, Universitat de Barcelona, Martì i Franquès 1, 08028 Barcelona, Spain
c) Centre for Advanced Study at The Norwegian Academy of Science and Letters, Drammensveien 78, 0271 N-Oslo, Norway
† corresponding author

We present an experimental study of the global velocity spatially averaged over the length scale ℓ, $V_\ell(t)$, of an air-liquid interface during the forced-flow imbibition of a viscous wetting liquid in a disordered medium. Thanks to a high resolution fast camera, we have followed directly the imbibition front and observed a complex dynamics, governed by power-law distributed avalanches on a wide range of durations and sizes [1, 2]. We characterize here this intermittent behavior by studying the statistical properties of the global velocity increments $\Delta V_\ell(\tau) \equiv V_\ell(t+\tau) - V_\ell(t)$ for various time lags τ. In particular we show that the shape of the PDF of $\Delta V_\ell(\tau)$ evolve with increasing τ from fat tail exponentially stretched PDFs towards a Gaussian PDF above a characteristic time τ_c, which corresponds to the characteristic avalanche duration.

Presentamos un estudio experimental de la velocidad global promediada espacialmente a escala ℓ, $V_\ell(t)$, de una interfaz aire-líquido en "embebimiento" a flujo constante en un medio desordenado de un líquido viscoso que moja el medio. Mediante una cámara de alta resolución hemos seguido directamente el frente de "embebimiento", observando una dinámica compleja gobernada por avalanchas distribuidas en ley de potencias en un amplio rango de duraciones y tamaños [1, 2]. Caracterizamos este comportamiento intermitente estudiando las propiedades estadísticas de los incrementos de la velocidad global $\Delta V_\ell(\tau) \equiv V_\ell(t+\tau) - V_\ell(t)$, para varios intervalos de tiempo τ. En concreto mostramos que la forma de la distribución de probabilidad de $\Delta V_\ell(\tau)$, a medida que τ aumenta, evoluciona de una distribución de colas largas a una distribución Gaussiana para τ mayor que un tiempo característico, τ_c, que corresponde a la duración característica de las avalanchas.

PACS: Fluctuation phenomena statistical physics, 05.40.-a; structure and roughness of interfaces, 68.35.Ct; fluid flow through porous media, 47.56.+r; fractals fluid dynamics, 47.53.+n

INTRODUCTION

Fluid invasion in disordered media -similarly to a wide variety of slowly driven heterogenous systems such as the motion of magnetic domain walls in disordered ferromagnets [3], wetting contact lines on rough substrates [4] or crack growth in heterogenous media [5, 6], exhibits a burst-like correlated dynamics spanning a very broad range of temporal and spatial scales [7-9]. Such a complex dynamics, generically referred to as "crackling noise", is the result of several competing forces acting at different length scales: while the fluctuations in capillary forces and the heterogeneous permeability destabilize the fluid interface, viscosity and surface tension damp the resulting interfacial fluctuations, leading finally to long-range correlations along the imbibition front. The correlation length, which measures the extent of the lateral correlations, is given by $\ell_c = \sqrt{\kappa / Ca}$, where κ is the permeability of the medium, and Ca the capillary number. As a consequence, imbibition fronts in a disordered medium undergo a complex kinetic roughening process characterized by an intermittent dynamics. In the limit $Ca \rightarrow 0$ the system displays critical interfacial fluctuations [10].

More specifically, using high resolution fast imaging in quasi two-dimensional forced-flow imbibition, we have shown recently that the front motion is driven by localized avalanches, power-law distributed both in sizes and durations, with exponentially decaying cutoffs that are related to the lateral correlations of the interface and diverge as the driving velocity decreases [2]. We demonstrated that the critical spatiotemporal dynamics observed during forced-flow imbibition can be described within the framework of a pinning-depinning transition. Moreover, we have shown that these local avalanches lead to a complex temporal activity of the global advancement of the front, with in particular large global velocity fluctuations that follow an asymmetric non-Gaussian distribution with a large exponential tail, due to the presence of spatial correlations along the front and finite-size effects [1, 11].

In the present work we go further on in the investigation of the global dynamics of imbibition fronts, and quantify the global intermittent behavior. Specifically, we analyze

the statistical properties of the global velocity increments $\Delta V_\ell(\tau) \equiv V_\ell(t+\tau) - V_\ell(t)$ for various time lags τ, and we show that the PDF of $\Delta V_\ell(\tau)$ evolves with increasing τ from fat tail exponentially stretched PDFs towards a Gaussian PDF above a characteristic time τ_c, which corresponds to the characteristic avalanche duration.

EXPERIMENTAL SETUP

The setup used in the present work (Fig. 1) has been previously described in Ref. [2]. It consists on a Hele-Shaw (HS) cell of 190 × 500 mm^2 (width × length), made of two parallel thick glass plates separated by a narrow gap spacing. We introduce dichotomic fluctuations in space of the gap thickness, $b = 0.46$ mm and $b - \delta b = 0.40$ mm. These spatial fluctuations are provided by copper patches of size 0.4×0.4 mm^2 and height $\delta b = 0.06$ mm, randomly distributed over a fiberglass substrate attached to the bottom plate and filling 35% of the total area. The patches do not overlap, and their orientation is shown in the bottom panel of Fig. 1.

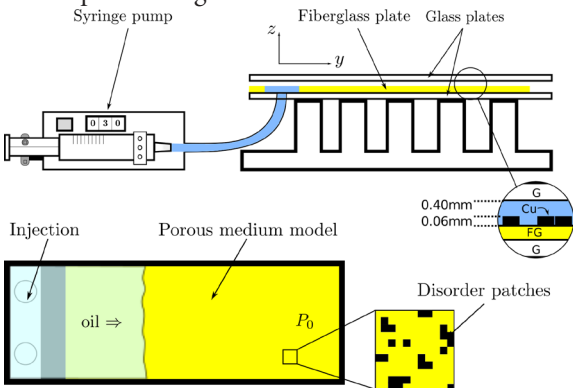

Figure 1: Sketches of the experimental setup. Top panel: the control parameter v is set by the syringe pump. The zoom on the right is a lateral view of the disordered HS cell, showing the parallel glass plates (G) and the fiberglass (FG) substrate with the copper obstacles (Cu). Bottom panel: sketch of the cell from top. The right end is open to air. The oil penetrates from the injection point at constant flow rate (constant average velocity v) and fills the porous medium model, displacing the resident fluid (air).The zoomed region shows the disorder patches and their orientation with respect to the fluid front.

We use a silicone oil (Rhodorsil 47V) as invading fluid, with dynamic viscosity $\mu = 52$ $mPa{\cdot}s$, density $\rho = 1000$ kg/m^3, and oil-air surface tension $\sigma = 20.7$ mN/m at room temperature (23 ^oC). The oil wets perfectly the glass plates, the copper patches and the fiber-glass substrate. The fluid is driven into the cell at a constant flow rate imposed by a syringe pump. Here, we will study the fluid invasion for one imposed flow rate corresponding to a mean front velocity $v = 0.131$ mm/s. Thus, both the local front height and the local velocity are correlated along the fluid interface up to the length scale $\ell_c = \sqrt{\kappa / (\mu v / \sigma)}$ = 7 mm, that corresponds to 5% of the system size $L = 136$ mm. We have performed 19 different experiments that explore various disorder realizations.

In the course of an experiment the interface propagates about 150 mm in the y direction before reaching a statistically stationary state with constant RMS fluctuations of the front height. The motion of the oil-air front is then recorded using a Motion Pro X3 plus video-camera with 1280 pixels in the transverse direction and 256 to 280 pixels in the direction of fluid advancement (y). The typical spatial resolution is $r = 0.106$ mm/pixel. We record about 10000 images per experiment at 100 fps (frames per second). An edge-tracking algorithm is applied to obtain the front position $h(x,t)$. In order to measure the local velocity $v(x, h(x,t))$ of the front we use a method developed for slow crack growth in heterogeneous materials [5], which consists on computing the waiting time $wt(x, y = h(x,t))$ that the front has spent on each position during its propagation. The local velocity map is then computed as $v(x, h(x,t)) = r/wt(x, y = h(x,t))$. Finally, from this local measurement, the global velocity of the front can be computed at any window size ℓ, as $V_\ell(t) = \frac{1}{\ell}\int_\ell v(x,t)dx$.

EXPERIMENTAL RESULTS

We will examine here the temporal fluctuations of the average velocity $V_\ell(t)$ as a function of the measuring window length scale ℓ. As shown on Fig. 3, even though the injection rate is constant, we observe that $V_\ell(t)$ is a jerky signal with a complex intermittent behavior characterized by very large positive fluctuations or avalanches [1]. We consider an avalanche as the occurrence of $V_\ell(t)$ above an arbitrary threshold, chosen here as the mean velocity $\langle V_\ell(t) \rangle$ (which would correspond to the imposed velocity v in an infinite system). We define the size S and duration T of an avalanche in the form shown in the bottom panel of Fig. 3. The avalanche size S represents the extra displacement of the average front within the duration T.

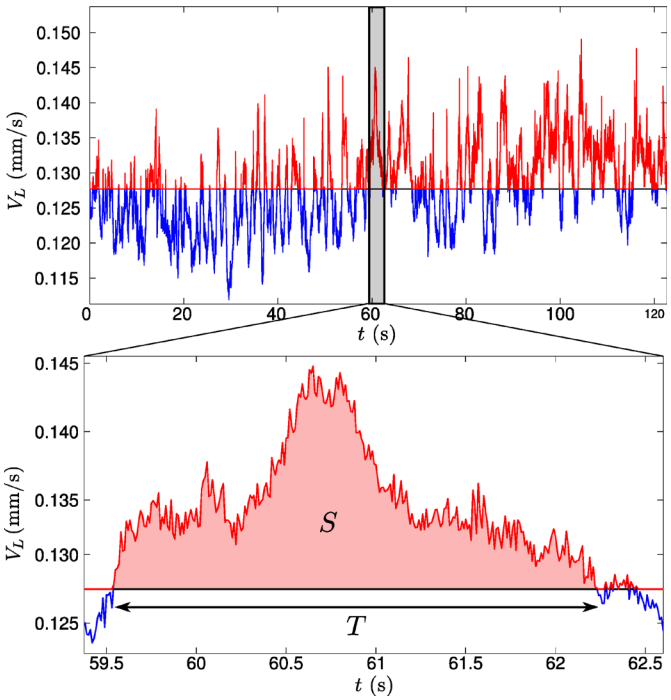

Figure 2: The top panel shows the global velocity signal for $\ell = L$, clipped by its average value. In the bottom panel a single avalanche is depicted, with size S and duration T.

We focus now on the statistics of avalanche durations in two

cases, depending on whether the global velocity V_ℓ is computed for $\ell < \ell_c$ or $\ell > \ell_c$. The corresponding distributions of avalanche durations are plotted in Fig. 3. In the top panel ($\ell > \ell_c$) we observe that the PDFs follow a power law with exponential cutoffs T_c that increase as the length of the measuring window ℓ is shortened towards ℓ_c. The inset shows the evolution of these cutoffs with ℓ. In the bottom panel ($\ell < \ell_c$), in contrast, the PDFs are exponential and do not evolve.

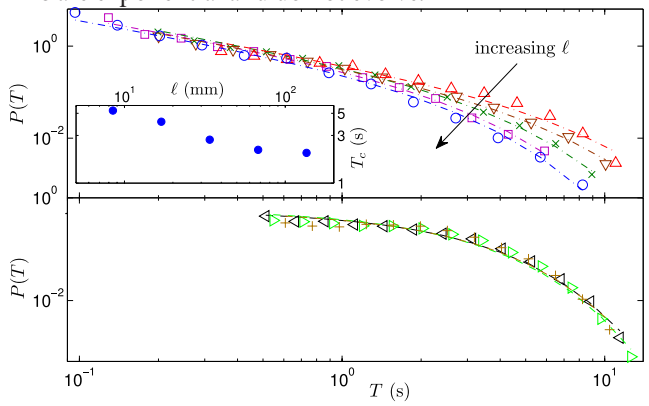

Figure 3: Top panel: PDFs of avalanche durations T, for window sizes $\ell = L/n$ ($> \ell_c$) with $n = 1, 2, 4, 8, 16$. Dashed lines are fits to power laws with exponential cutoffs. In the inset the cutoff duration T_c is plotted as a function of ℓ. Bottom panel: PDFs of avalanche durations T, for window sizes $\ell = L/n$ ($< \ell_c$) with $n = 32, 40, 50$. Dashed lines are fits to decaying exponentials with nearly the same characteristic duration $T_c = 2.06 \pm 0.06$.

In order to study the temporal fluctuations of $V_\ell(t)$, we analyze the statistical properties of the global velocity increments $\Delta V_\ell(\tau)$ for various time delays τ, and observation length scales ℓ. Such analysis has been originally proposed to study the intermittent behavior of turbulent flows [12]. We show on Fig. 4 the distributions of the normalized velocity increments $Y \equiv (\Delta V_\ell - \langle V_\ell \rangle)/\sigma_{\Delta V_\ell}$ for logarithmically increasing time lags τ and the global velocity measured at $\ell = L/8$. Interestingly, we observe that the shape of these distributions evolves through the temporal scales τ from fat tail exponentially stretched distributions at small time lags towards Gaussian distributions above a characteristic time τ_c. Such behavior is indicative of the intermittent character of the fluid invasion process, and uncovers complex temporal correlations [12-14] for durations shorter than τ_c.

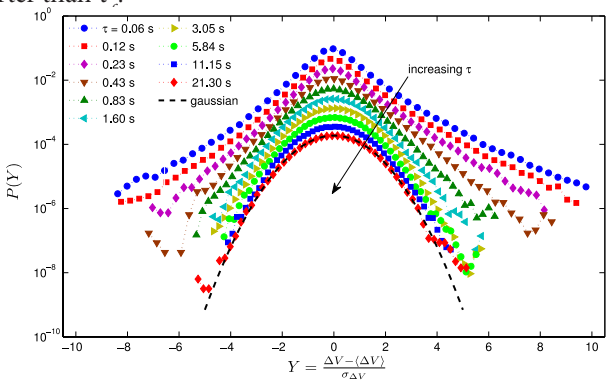

Figure 4: Semilog plot of $P(Y)$ vs $Y \equiv (\Delta V_\ell - \langle V_\ell \rangle)/\sigma_{\Delta V_\ell}$ (dotted lines) for increasing time lags τ and for $\ell = L/8$, shifted vertically for visual clarity. The PDFs evolve from fat tail distributions for $\ell < \ell_c$ to Gaussian distributions for $\tau > \tau_c \simeq 2$ s. A Gaussian PDF (dashed line) is also plotted as a guide to the eye.

To characterize and quantify the flatness of these PDFs, we compute the kurtosis $k \equiv E(x - \langle x \rangle)^4/\sigma^4$ of the distributions $P(\Delta V_\ell(\tau))$, where E stands for the expected value. On Fig. 5 we represent the kurtosis vs. the time lag τ, varying systematically the measuring window size ℓ. We observe that the kurtosis decreases systematically as τ and ℓ increase. Above a characteristic duration τ_c it converges to the value $k_G = 3$ of a Gaussian signal whenever $\ell > \ell_c$, in agreement with the result of the previous Fig. 4. In contrast, for $\ell < \ell_c$ the kurtosis at large τ saturates to $k > k_G$, implying that the underlying statistics is not Gaussian. Below τ_c, the increase of the kurtosis at progressively shorter temporal scales seems to be close to a power law $k \propto \tau^{-\alpha}$. The power-law exponent α measures the intermittency strength of the global velocity at short durations [14]. Its evolution with the measuring window length scale is reported in the inset of Fig. 5.

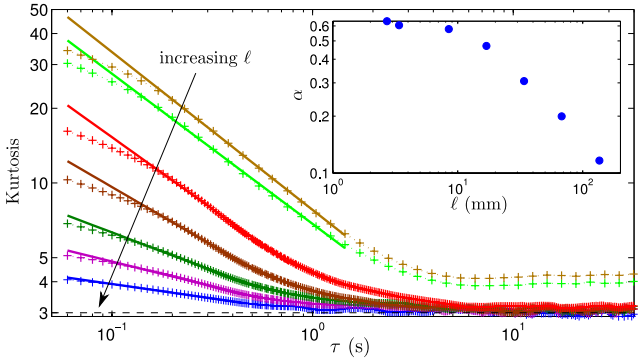

Figure 5: Kurtosis of $\Delta V_\ell(\tau)$ for $\ell = L/n$ and $n = 1, 2, 4, 8, 16, 40, 50$, in log-log scale. The kurtosis is a measure of the flatness of the distribution. The dashed line represents the value for a Gaussian distribution, $k_G = 3$. Solid lines are power-law fits, $\tau^{-\alpha}$, for small τ. Inset: exponent α as a function of ℓ.

Finally, we have extracted the characteristic time τ_c at which the kurtosis flattens out. Interestingly, the values of τ_c and especially their evolution with the measuring window size ℓ appear very close to the typical durations of the global avalanches, defined as $\langle T \rangle$. This similar trend is shown in Fig. 6.

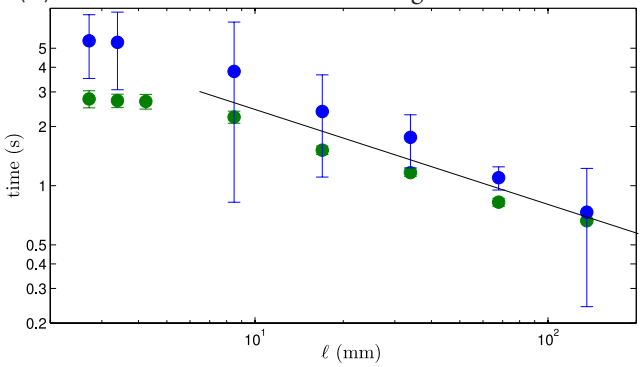

Figure 6: Characteristic times τ_c and $\langle T \rangle$ vs ℓ in log-log scale. The values of τ_c (squares) are obtained from analyzing the kurtosis of $P(\Delta V_\ell(\tau))$ with $\ell = L/n$ and $n = 1, 2, 4, 8, 16, 40, 50$. Those of $\langle T \rangle$ (circles) are the mean duration of avalanches for $\ell = L/n$ and $n = 1, 2, 4, 8, 16, 40, 50$. The solid line is plotted as a guide to the eye for $\ell > \ell_c$.

CONCLUSIONS

By analyzing the statistical behavior of the differences in the global velocity of imbibition fronts in time lapses τ and

observation windows ℓ, we have shown that the dynamics displays the characteristic features of an intermittent process. The shape of the PDF of $\Delta V_\ell(\tau)$ evolves with increasing τ from a fat tail exponentially stretched PDF to a Gaussian PDF above a characteristic time τ_c, which corresponds to the characteristic avalanche duration.

[1] R. Planet, S. Santucci and J. Ortín, Phys. Rev. Lett. **102**, 94502 (2009).
[2] S. Santucci, R. Planet, K. Jørgen Måløy and J. Ortín., Europhys. Lett. **94**, 46005 (2011).
[3] G. Durin and S. Zapperi, Phys. Rev. Lett. **84**, 4705 (2000).
[4] E. Rolley, C. Guthmann, R. Gombrowicz and V. Repain, Phys. Rev. Lett. **80**, 2865 (1998).
[5] K. J. Måløy , S. Santucci, J. Schmittbuhl and R. Toussaint, Phys. Rev. Lett. **96**, 045501 (2006).
[6] D. Bonamy, S. Santucci and L. Ponson, Phys. Rev. Lett. **101**, 045501 (2008).
[7] M. Kardar, Phys. Rep. **301**, 85 (1998).
[8] D. S. Fisher, Phys. Rep. **301**, 113 (1998).
[9] J. P. Sethna, K. A. Dahmen and C. R. Myers, Nature **410**, 242 (2001).
[10] M. Alava, M. Dubé and M. Rost, Adv. Phys. **53**, 83 (2004).
[11] R. Planet, S. Santucci and J. Ortín, Phy. Rev. Lett. **105**, 029402 (2010).
[12] B. Castaing, Y. Gagne and E. J. Hopfinger, Physica D 46, **177** (1990).
[13] E. Bertin, Phys. Rev. Lett. **95**, 170601 (2005).
[14] L. Chevillard, B. Castaing, A. Arneodo, E. Leveque, J. -F. Pinton and S. Roux, arXiv:1112.1036 (2011).

NUMERICAL STUDIES OF AEROFRACTURES IN POROUS MEDIA

ESTUDIOS NUMÉRICOS DE AEROFRACTURAS EN MEDIOS POROSOS

M. J. Niebling[a,b,c †], R. Toussaint[b,c,d], E. G. Flekkøy[a,d] and K. J. Måløy[a,d]

a) Department of Physics, University of Oslo, P.O. Box 1048, 0316 Oslo, Norway, Michael.Niebling@fys.uio.no†
b) Institut de Physique du Globe de Strasbourg, CNRS
c) University of Strasbourg, 5 rue Descartes, 67084 Strasbourg Cedex, France
d) Centre for Advanced Study at the Norwegian Academy of Science and Letters, Drammensveien 78, 0271 Oslo, Norway
† corresponding author

During the hydraulically induced compaction of a granular layer fracture patterns arise. In numerical simulations we study how these patterns depend on the gas properties as well as on the properties of the porous medium. In particular the relation between the speed of fracture propagation and injection pressure is here studied in detail.

Durante la compactación hidráulicamente inducida de una capa granular surgen patrones de fractura. En éste artículo estudiamos cómo éstos patrones dependen tanto de las propiedades del gas como de las del medio, utilizando simulaciones numéricas. En particular, estudiamos en detalle la relación entre la presión de inyección y la velocidad de propagación de la fractura.

PACS: Pattern formation in complex systems, 89.75.Kd; flow through porous materials, 47.56.+r; compressible flows, 47.40.-x

INTRODUCTION

Stress induced by fluid or gases can cause diverse materials to break and fracture. Such hydraulic fractures are a natural and common phenomenon in the field of volcanism and are artificially initiated to enhance the recovery of natural gas and mineral oil by fracturing the reservoir rock with pressurized fluids. Recently a new perspective on hydrofractures was added with the storage of supercritical CO_2 attracting the interest of an increasing number of researchers. In this respect two scenarios are considered. First it is one option to inject CO_2 into existing hydrofractures, and second the injection of the CO_2 can create additional fractures [1, 2]. The typical components for such fractures are a porous material and a compressible gas. Injection of pressurized fluids in a porous material, deforming beyond the elastic limit, has been studied in granular materials in Hele-Shaw cells, [3–8], with the injection of air or oil in systems with open boundary conditions, and during cyclic loading [9]. It was also studied in systems with a confinement for the grains, prevented from getting out of the cell, which allowed to observe the formation of thin fractures [10]. In this paper [10] it was found and discussed a criterion that the porous media and the fluid need to fulfill to allow the formation of fractures. For this purpose the gas' viscosity was varied. It was further discussed how the shape of the fractures depend on the properties of the porous material and of the injected gas in simple 2 dimensional (2D) numerical simulations.

In contrast to the previous article we will not change the properties of the injected gas or the porous material in this present article. Here we explore in particular the effect of the amplitude of the gas pressure imposed in the source on the fracture morphology. Furthermore, all simulations here will be ran in a regime where fractures are created.

SIMULATION SETUP

As shown in Fig. 1 the setup consists of a cell with two glass plates separated by 1 *mm*. The gap between the plates is filled with particles. The empty space between the grains is saturated with a fluid that has the same properties as the fluid that is injected. Consequently, the only two media involved in the dynamics are the grains and the fluid. At the start of the simulations the average solid volume fraction of the grains is $\rho_s^{(0)} = 0.42$. This starting solid volume fraction is homogeneous with negligible density fluctuations although the particles are at random positions. The value of $\rho_s^{(0)} = 0.42$ is chosen to be less than the possible maximum of $\rho_s^{(\max)} = 0.60$ to allow compaction of the grains. On the inlet side of the cell the pressure is increased gradually in a set of six different simulations from a value of $P_I = 0.5 \times 10^5$ *Pa* to a value of $P_I = 2.5 \times 10^5$ *Pa* above the atmospheric pressure of $P_0 = 1.0 \times 10$ *Pa*. On the opposing side to the inlet the cell has an open boundary for the fluid but particles are not able to leave the cell here. In a real experiment, this could be achieved by using a net with a mesh smaller than the particles. The remaining boundaries are completely sealed for both media. In the simulation around 200 000 grains of diameter 140 ± 10% μm are involved. Finally, the pressure at the inlet is increased and maintained as a step function in time, at a steep ramp, and particles hardly move before the maximum injection pressure P_I is reached.

THEORY AND MODEL

Using a well tested numerical model we have the freedom to explore the parameter space independently. The details of the method can be found in [6, 11-17], and alternative models can be found in [18-22]. The model describes the fluid in terms of a pressure field while the porous medium is modeled by simulating discrete particles.

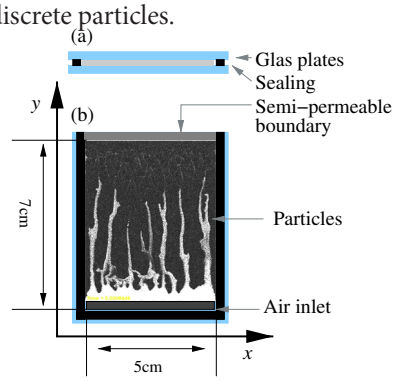

Figure 1: Numerical setup of the system.

THEORY AND SIMULATIONS

Dynamics of the gas phase. The equation for the evolution of the pressure $P = \tilde{P} + P_0$, where P_0 is the atmospheric pressure and $\tilde{P}$ the local pressure fluctuations is given by

$$\phi\left[\frac{\partial P}{\partial t} + \boldsymbol{u}\cdot\nabla P\right] = \nabla\cdot\left[P\frac{\kappa}{\mu_f}\nabla P\right] - P\nabla\cdot\boldsymbol{u} \qquad (1)$$

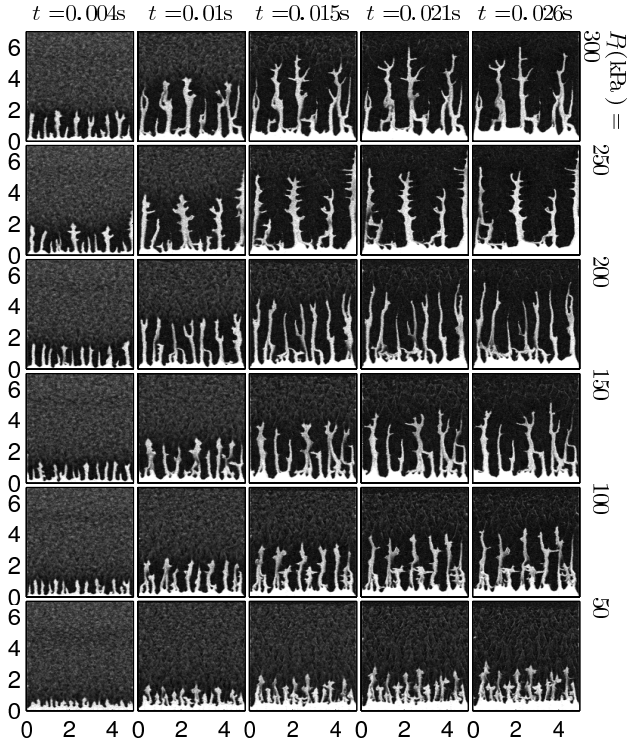

Figure 2: Snapshots during the simulations of the particle density in the Hele-Shaw cell, displayed for decreasing injection pressure P_I from top to bottom and as a function of time (left to right). Low particle density appears brighter in the snapshots. Under air injection, fractures, fingers and dispersed bubbles of low particle density emerge and propagate. *x*- and *y*-axis units are given in *cm*. The *y*-axis specifies the distance from the inlet.

In this equation, the pressure is described in terms of the local granular velocity $\boldsymbol{u}$, the viscosity μ_f of the gas, the local porosity $\phi = 1 - \rho_s$ and the local permeability κ. Eq. (1) is derived from mass conservation of the gas and the granular medium and by assuming a local Darcy law.

Dynamics of the particles. For the particles we basically use Newton's second law

$$m\frac{dv_p}{dt} = \boldsymbol{F_I} + \boldsymbol{F_d} + \boldsymbol{F_a} - \frac{\nabla P}{\rho_n}, \qquad (2)$$

with particle velocity v_p, particle mass m, particle mass density ρ_m, cell spacing h and the number density $\rho_n = \rho_s\rho_m/m$. $\boldsymbol{F_I}$ are linear inter-particle solid contact forces. $\boldsymbol{F_d}$ is a viscous damping force during particle collisions. For F_a, the interaction with the side plates we assume that the normal stress $P_g^{\perp}$ in the granular packing is proportional to the in-plane stress $P_g^{\parallel}$ by a factor λ (Janssen hypothesis). Using further a Coulomb friction model we state that the frictional force F_a per particle with the glass plates is proportional to the normal stress by a friction coefficient γ. With these two assumptions we find an expression for the friction force with the side plates.

$$F_a \le \gamma S_a(2P_g^{\perp} + \rho_m gh) = \gamma S_a(2\lambda P_g^{\parallel} + \rho_m gh). \qquad (3)$$

$S_a = \pi a^2$ is the contact area of the particles with the plates.

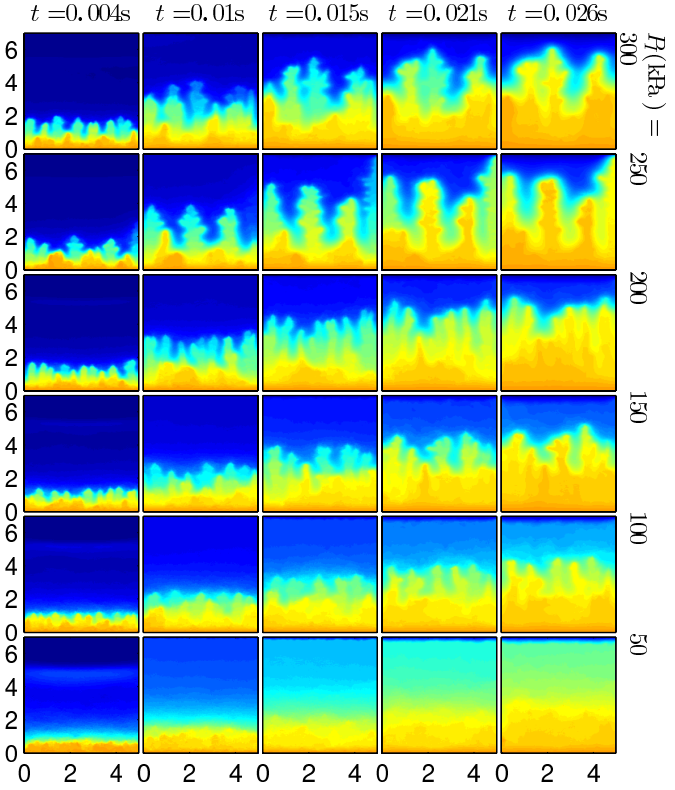

Figure 3: The pressure evolution for decreasing injection pressure P_I (top to bottom) and as a function of time (left to right). High pressure appears yellow (brighter) in the snapshots. *x*- and *y*-axis units are given in *cm*.

RESULTS

We ran a set of six simulations for injection pressures of P_I = (0.5, 1.0, 1.5, 2.0, 2.5, 3.0) × 10^5 *Pa* above atmospheric pressure P_0, a fluid viscosity of μ_f = 18.0 *mPa·s* and a friction

coefficient with the side plates of $\gamma\lambda = 4.0$. The injected gas is considered as an ideal gas and has the compressibility of air $\beta_T = 1/P_0$ at P_0. The value of P_I at the inlet is reached very fast and particles start to move shortly after. During this compression of the particles fractures emerge in the granular packing. In Fig. 2 a set of snapshots of the particle density is shown. The snapshots are taken at increasing time from left to right. Each horizontal row of pictures corresponds to one of the six simulations at a different injection pressures. In Fig. 3 snapshots of the corresponding pressure field in the cell are displayed. The pressure field is normalized to one to allow a qualitative comparison.

In these plots an apparent feature is the different propagation speed and position of the emerging fractures. A high injection pressure causes the fractures to propagate faster. To quantify this observation we can plot the position of the most advanced finger tip as a function in time. This is done in Fig. 4. The plot clearly proves the previous observation. Furthermore it turns out that the systematic increase of the propagation speed is also proportional to the square root of the injection pressure. This is checked in Fig. 5. Here the rescaling of the fracture tip position by the square root of the injection pressure $\sqrt{P_I}$ results in a collapse of the graphs. The disagreement at the later stages of the simulations in this plot results from the finite size of the system, which allows fractures to grow only up to a certain size. Finally we can state that the fingers grow according to

$$Y_t = \sqrt{P_I}\, f(t), \tag{4}$$

where $f(t)$ is a function which appears in the plots to be almost linear at early stages of the finger growth for $t < 0.01\ s$.

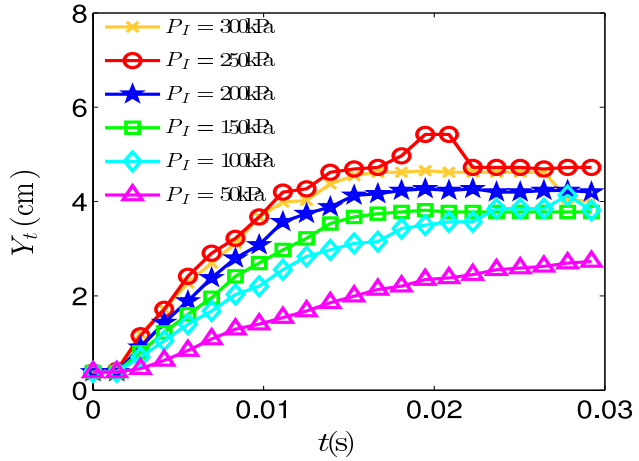

Figure 4: The position of the most advanced finger/fracture as a function of time at different injection pressure P_I. The higher the injection pressure P_I the further fingers grow.

In Fig. 2 we also observe that the fingers at high injection pressure propagate further into the packing before complete compaction of the grains takes place. This can be also seen in Fig. 4 where the finger position stops growing at longer distances from the inlet the higher the injection pressure is.

Apart from the finger position, the increase of the injection pressure also affects the shape of the fingers. In Fig. 2 it can be seen that the fingers get more branched and fracture-like at higher injection pressure. At low injection pressure fingers appear to be straighter while increasing the injection pressure, fingers develop more and more branches. At the highest injection pressure of $P_I = 3.0 \times 10^5\ Pa$ the fingers clearly show characteristics of fractures.

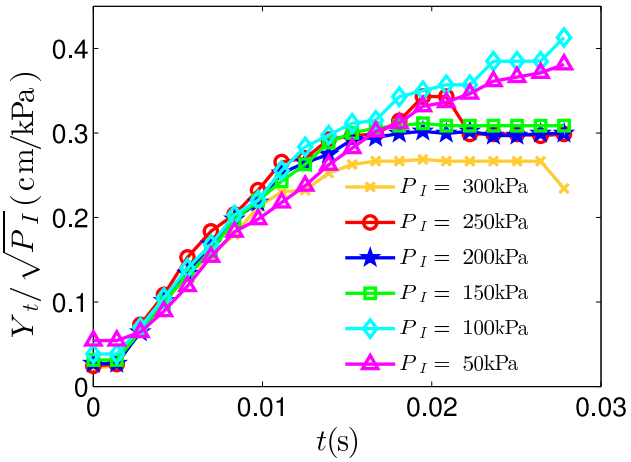

Figure 5: The position of the most advanced finger/fracture rescaled by the square root of the injection pressure $\sqrt{P_I}$. As a function of time the graphs at different injection pressure P_I collapse onto a single graph.

At high injection pressure P_I the pressure gradients are the largest. When the boundary is deformed the expected changes of the pressure gradients are therefore also higher at high injection pressure than at low injection pressure. At low P_I, one expects a lower pressure gradient everywhere, and thus a low effect of seepage forces and a slower deformation. Leading to overall smoother pressure gradients and a more stable front deformation. We thus expect faster finger propagation, and more branching at a higher injection pressure.

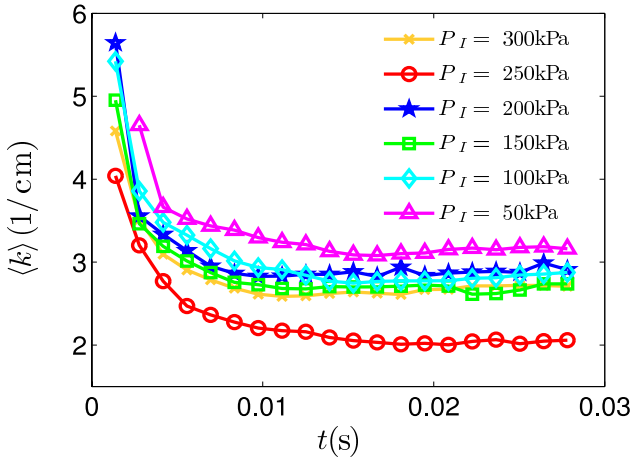

Figure 6: The average of the spatial finger wavenumber in x direction.

Finally also the spatial distance between the fingers depends on the injection pressure (see Fig. 6). At low injection pressure the number of fingers is higher than at high injection pressure, as can be also seen in Fig. 2. In general the finger spatial frequency decreases in time after injection has started and fingers propagate through the cell. This can be shown by calculating the average of the characteristic spatial finger wavenumber in x direction. First the power spectrum S_j of each horizontal line j of the particle density is calculated. Taking the average of these power spectra results in a single power spectrum $\overline{S}$. From this